High Capacity Li^+ Storage through Multielectron Redox in the Fast-Charging Wadsley–Roth Phase $(W_{0.2}V_{0.8})_3O_7$

Kira E. Wyckoff,[†,⊥] Daniel D. Robertson,[‡,⊥] Molleigh B. Preefer,[¶] Samuel M. L. Teicher,[†] Jadon Bienz,[¶] Linus Kautzsch,[†] Thomas E. Mates,[†] Joya A. Cooley,[§] Sarah H. Tolbert,[*,‡,∥] and Ram Seshadri[*,†,¶]

†*Materials Department and Materials Research Laboratory*
University of California, Santa Barbara, California 93106, United States
‡*Department of Chemistry and Biochemistry*
University of California, Los Angeles, California 90095, United States
¶*Department of Chemistry and Biochemistry*
University of California, Santa Barbara, California 93106, United States
§*Department of Chemistry and Biochemistry*
California State University, Fullerton, California 92831, United States
∥*Department of Materials Science and Engineering*
University of California, Los Angeles, California 90095, United States
⊥*Contributed equally to this work*

E-mail: tolbert@chem.ucla.edu; seshadri@mrl.ucsb.edu

Abstract

The Wadsley–Roth phase $(W_{0.2}V_{0.8})_3O_7$, crystallizing in a structure obtained through crystallographic shear of $3\times3\times\infty$ ReO_3 blocks, is a somewhat rare exemplar for this class of compounds in that it contains a relatively small amount of 4d and/or 5d transition elements. Here we demonstrate that it functions as a high-rate, high-capacity material for lithium ion batteries. Electrochemical insertion and de-insertion in micron sized particles made by conventional solid-state preparation and in sub-100 nm particles made by combining sol-gel precursors with freeze-drying methods, indicate good rate capabilities. The materials display high capacity — close to 300 mAh g^{-1} at low rates — corresponding to insertion of up to 1.3 Li per transition metal at voltages above 1 V. Li insertion is associated with multielectron redox for both V and W observed from ex-situ X-ray photoelectron spectroscopy. The replacement of 4d and 5d elements with vanadium results in a higher voltage than seen in other, usually niobium-containing shear-structured electrode materials, and points to new opportunities for tuning voltage, electrical conductivity, and capacity in compounds in this structural class.

Introduction

The ability to tune the chemistry of electrode materials across multiple length scales provides opportunities for developing electrodes for a variety of Li–ion battery applications, ranging from portable electronics, to electric vehicles, and grid-scale storage.[1,2] Research on Li-ion battery technology has particularly focused on improving both the energy density and rate capabilities of electrode materials.[3] Materials capable of being charged in the course of minutes as opposed to hours, could have important ramifications across a broad range of applications. For many currently used and studied materials, fast charging is hindered due to intrinsic materials properties often associated with the crystal structure, namely the ease of ion and electron transport, structural and electronic phase transitions *etc.*. A common work-around to address limited ion mobility has been to optimize parti-

cle morphology through meso- and nanostructuring,[4,5] with the goal of decreasing Li–ion diffusion distances within the particle, sometimes with concomitant suppression of phase transitions.[6–9] Carbon additives and carbon-coating has also been frequently employed to overcome inherently poor electron transport.[10,11] These impressive feats of engineering, exemplified by materials such as $LiFePO_4$,[10,11] have allowed for broad adoption of Li–ion batteries in many applications, but the search for new materials continues.

Anode materials with voltages close to 0 V *vs.* Li/Li^+, while providing the greatest energy density, are contraindicated for high-rate applications. Graphite for example, effectively transports Li^+ ions and electrons but is associated with detrimental electrolyte reactions,[12] dendrite formation that leads to thermal runaway,[13–15] and volume expansion that leads to particle fracture.[16] Highly engineered (*ie.* nanoscaled and carbon-coated) $Li_4Ti_5O_{12}$ with a higher average voltage of 1.5 V has good capacity retention at high rates.[17] The higher voltage minimizes dendrite growth but the costs associated with elaborate electrode preparation decreases widespread adoption.[18]

The focus of this work are on materials that possess crystallographic shear. These are structures that derive from anion vacancies that are accommodated through shear of the basic polyhedral structural motifs. First described by Magnéli,[19] the process of shear results in greater sharing of anions between polyhedra. A class of materials that possess such crystallographic shear are the so-called Wadsley–Roth family of compounds, which have shear structures described as blocks of corner-connected MO_3 octahedra. These generally comprise oxides of early transition metals such as Ti, V, Nb, Mo, and W.[20–23] While the earliest reports on these structures were based on electron diffraction and model-building, neutron diffraction has revealed the most intricate structural details.[24,25]

Early studies on Li insertion in this class of materials showed that a broad array of compositions could be used as electrodes.[26–30] The utility of $TiNb_2O_7$ was rediscovered by Goodenough and coworkers.[31,32] Recent studies have demonstrated that large micron-sized particles of the shear structured phases $Nb_{12}WO_{33}$,[33] H–Nb_2O_5,[34,35] $TiNb_{24}O_{62}$,[36]

$Nb_{16}W_5O_{55}$,[37] $TiNb_2O_7$,[38] $MoNb_{12}O_{33}$,[39] and PNb_9O_{25},[40] are all capable of impressive lithium storage capacity at high cycling rates.

From a design perspective, compounds displaying features of crystallographic shear are exciting because they contain specific structural motifs that allow for excellent Li–ion diffusion and the potential for electron delocalization. The compounds typically possess some combination of edge- and corner-connected octahedra. How these combine in the structure, along with the specific chemical composition, critically impacts electrochemical performance. The edge-sharing octahedra allow for electron delocalization pathways while also providing structural integrity.[41] This integrity protects against octahedral tilting and rotation seen in pure ReO_3 structures (all corner– and no edge–sharing) that are detrimental to reversible cycling.[26,29,42] However the corner connectivity deriving from the ReO_3 blocks also plays an essential role in creating channels that facilitate ion insertion and transport. Evidence from NMR, magnetism, and conductivity measurements confirms that these structural features contribute to low activation barriers for lithium diffusion.[35,36,38,40,43] These materials are additionally compelling because of their high capacities. This is due in large part to the fact that these materials comprise of early transition metals capable of multi-electron redox, where it is possible to insert more than 1 Li per transition metal.

While many Wadsley–Roth phases contain Nb, V-containing phases appear to have been much less studied, despite the fact that vanadium is more earth-abundant and more geographically and industrially widespread, compared to niobium.[44] Here we characterize the electrochemical insertion properties of the Wadsley–Roth phase $(W_{0.2}V_{0.8})_3O_7$, whose crystal structure is depicted in figure 1. First reported by Galy in 1972, the crystallography of this $3\times3\times\infty$ block structure was determined from single-crystal studies.[45] From the viewpoint of composition, this is an interesting compound since the closest vanadium phase to V_3O_7 is formed under high-pressure with a distinctly different structure,[46] and a W_3O_7 phase does not appear to have been reported. There is a high likelihood that $(W_{0.2}V_{0.8})_3O_7$

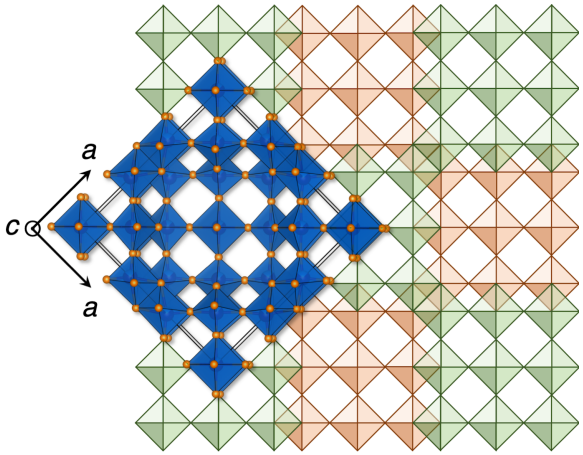

Figure 1: Crystal structure of $(W_{0.2}V_{0.8})_3O_7$ (space group is I_4/mmm, No. 139) comprising of $3\times3\times\infty$ blocks of corner-connected (W,V)O_3 octahedra, offset and connected through edge-sharing (shear planes). The real structure is overlaid onto a schematic that depicts the arrangement of the 3×3 blocks. The two different colors employed for the blocks of octahedra are used here to indicate that they are offset along the c direction.

is stabilized by configurational entropy, as suggested by Navrotsky and coworkers for related phases.[47]

Early studies examined related compounds as electrodes,[27,28,30] but not for high-rate performance. Here, using both small particles prepared through a solution freeze-drying method, and conventionally prepared larger particles, we develop an understanding of the intrinsic capabilities of the materials for Li storage. Reversible and stable cycling at rates up to 20C are demonstrated. The relatively minor perturbation of the structure arising from Li insertion is confirmed with *operando* X-ray diffraction. Ex-situ X-ray photoelectron spectroscopy studies show reduction of the transition metals, respectively to V^{3+} and W^{4+}, explaining the relatively high capacity. Despite the competitive capacity retention in bulk particles of $(W_{0.2}V_{0.8})_3O_7$, there are kinetic advantages displayed by the smaller particles made by the solution freeze-drying route, particularly at intermediate rates.

The materials studied here differentiate themselves from other Wadsley–Roth phases in that they are not fully oxidized even in the pristine, delithiated state, which contributes to some electronic conductivity prior to lithium insertion. Additionally, the compound stores charge at voltages higher than found in related structures and provides the basis for

exploration of voltage tuning within the family of crystallographic shear structures.

Experimental Section

The title material was conventionally prepared (labelled Conv.) through solid-state methods. Stoichiometric quantities of WO_3 (Sigma Aldrich, 99.9 %), V_2O_5 (Materion, 99.9 %), and V_2O_3 (Strem Chemicals, 95 %) were ground together and pressed into pellets weighing between 250 mg and 300 mg. The pellets were then placed in a vitreous silica tube and sealed with a methane-oxygen torch, evacuated three times, and subsequently filled with 40 mm Hg partial pressure of Ar. The tube was annealed in a furnace at 700°C for 24 h followed by a water quench to room temperature. Small particles were prepared by freeze-drying (henceforth labelled FD) a stoichiometric solution of precursors and subsequently calcining under flowing Ar. In a typical preparation, 200 mg of NH_4VO_3 and 105 mg of $(NH_4)_{10}(H_2W_{12}O_{42})$ were added to 5 cm^3 of distilled water and heated until the solids were fully dissolved. The resulting yellow solution was added drop-wise to liquid N_2. After removal of the remaining liquid N_2, the frozen solution was subjected to vacuum ($<$100 mTorr) on a Schlenk line for 10 h to 20 h to remove water. Once dry, the powder was calcined in flowing Ar in a tube furnace at 700°C for 1 h (30°C per min ramp rate). The furnace was then cooled to room temperature. The obtained particles were stored under inert atmosphere to prevent unwanted surface oxidation.

Both materials were cast on copper foil in an 80:10:10 (wt-%) ratio of active material:conductive carbons:polyvinylidene fluoride. Cycling of the Conv. material employed carbon black (TIMCAL Super P) while for the FD material, a 50:50 mixture of carbon nanotubes and carbon nanofibers were used. The active material was ball milled for 30 min in a 2 cm^3 canister with the appropriate amount of carbon based additives. This mixture was combined with PVDF dissolved in NMP to form a slurry that was mixed in a FlackTek speed mixer at 2000 rpm for 30 min. A 120 μm doctor blade was used to cast the material

onto copper foil, and this film was dried at 110°C under vacuum for 2 h. The electrodes were punched as 10 mm diameter disks with a loading of 1 mg cm^{-2} to 2 mg cm^{-2}.

All electrochemical cells were fabricated in an Ar-filled glovebox. Unless noted otherwise, Swagelok cells were employed with 1 M $LiPF_6$ in EC/DMC 50/50 v/v (Sigma Aldrich) with a polished Li foil counter electrode and a glass fiber separator (Whatman GF/D). Cells were discharged to 1 V and charged to 3.2 V. All electrochemical experiments were performed using BioLogic potentiostats.

The compound $(W_{0.2}V_{0.8})_3O_7$ can be considered to comprise $0.6WO_3$ + $1.6VO_2$ + $0.8VO_{2.5}$. W can be reduced to the 4^+ state and V to the 3^+ state (as we shall also demonstrate presently), so on this basis, 4.4 electrons (along with the corresponding Li^+ ions) can in principle be incorporated. However, following the usual convention for this class of materials, C-rates were calculated based off the reduction of one electron per redox-active transition metal. In this case, 3 Li were assumed to insert into the crystal structure for calculating C rates, *eg.* C/5 = $3Q/5$ = 233 mAh g^{-1}/5 h = 46.6 mA g^{-1}, where Q is the charge.

Electrochemical impedance spectroscopy was carried out on a BioLogic VSP potentiostat/galvanostat. Impedance measurements were performed on two-electrode coin cells between 900 kHz and 100 mHz using a 10 mV input. Impedance spectra were collected at every 0.2 V vs. Li/Li^+ between +1.0 V and +3.2 V vs. Li/Li^+ on electrodes that had been previously cycled with galvanostatic rate testing between +1.0 V and +3.5 V vs. Li/Li^+. A one hour potentiostatic hold was applied before impedance measurements, during which the current dropped below 50 μA/g.

Powder diffraction data to establish sample purity were collected on a Panalytical Empyrean diffractometer with a CuK_α source (λ = 1.5406 Å). The materials were ground and loaded on a silicon zero diffraction plate. Rietveld refinements to the previously published structure[45] were carried out with TOPAS.[48] VESTA was used for visualization of the crystal structure.[49]

Particle sizes and morphologies were studied using an FEI Apreo C scanning electron microscope. The powder samples were pressed onto double-sided copper tape and sputter-coated with gold for 60 s. Images were collected with a voltage of 15 kV and a current of 0.8 nA.

For *operando* X-ray diffraction, the electrode mixture was pressed into a 15 mm diameter pellet and placed into a custom electrochemical cell with a Be window. A glass fiber separator (Whatman, GF/D) was soaked in 1 M $LiPF_6$ (Sigma Aldrich), and the counter electrode was a polished Li metal disc pressed into a stainless steel current collector. The cell was cycled galvanostatically at a rate of C/10 (assuming 3 Li per formula unit) for one complete cycle. X-ray diffraction patterns were collected repeatedly using the Panalytical Empyrean diffractometer referenced above, from $2\theta = 13^\circ$ to 50° over 17 min. intervals. The amorphous background (due to the glass fiber separator) and the signal for each scan was separately smoothed and fit using Tikhonov regularization.[50].

Samples for X-ray photoelectron spectroscopy (XPS) were prepared by discharging/charging the cast electrodes described earlier to the desired voltages in a Swagelok cell. These cells were then disassembled inside of an Ar-filled glovebox, the electrodes were removed and washed for 2 hours in dimethyl carbonate to remove $LiPF_6$ from the electrolyte, with subsequent centrifuging and drying in the glovebox atmosphere overnight. A section of the electrode was cut and the copper foil side of the disk was gently pressed onto the XPS sample holder using double-sided tape. A custom-built, capped XPS holder was used, equipped with a Viton seal and a screw-down lid that could be removed after the sample achieved vacuum in the XPS antechamber. All samples were measured using a Thermo Fisher Escalab Xi^+ XPS equipped with a monochromatic Al anode ($E = 1486.7$ eV). Samples were etched using a cluster gun for 40 s to clean the surface and improve count intensity. Survey scans were measured at 100 eV pass energy, and high-resolution scans were measured in the V $4p$, W $4f$, and Li $1s$ regions at 20 eV pass energy. Ex-situ spectra were referenced to the F $1s$ peak from LiF at 685.5 eV and the pristine spectrum was referenced to adven-

titious carbon at 285 eV.[51–53] CasaXPS was used to fit the data using Shirley backgrounds and GL(30) peak shapes. High resolution scans of V and W were fit using appropriate spin-orbit splitting and peak area ratios.[54]

Density functional theory (DFT) – based electronic structure calculations were performed using the Vienna ab initio Simulation Project VASP v5.4.4[55–57] employing projector augmented wave potentials[58,59] with energy convergence better than 10^{-6} eV. PAW potentials were selected based on the version 5.2 recommendations. Simulations were found to be well-converged for an energy cutoff of 500 eV and an automatically generated k-mesh with the length-density parameter $\ell = 50$ ($\ell = 50$ corresponds to 14×5×5 and 4×4×13 Γ-centered meshes for the primitive cell and the conventional cell displayed in the text, respectively). PBE[60] and SCAN[61] functionals were employed for calculations on the V_3O_7 model structure. The SCAN functional often provides improvements over PBE accuracy for systems with localized electrons, and previous studies have found improvements with SCAN estimates of magnetic moments specifically for transition metal oxide battery materials.[62] However, in these simulations, for ferromagnetic initialization with and without spin-orbit coupling, we find no stable magnetization in either structure regardless of functional choice. PBE and SCAN densities of states (DOS) and charge densities are visually indistinguishable and only the results obtained with the SCAN functional are reported in the text. The projected density of states was post-processed using LOBSTER.[63–66] Mapping of the bond valence in the space of the crystal structure was carried out using the script PyAbstantia.[67] All visualization involving crystal structures were carried out using VESTA.[49]

Results and discussion

Preparation of the Conv. material through the solid state methods described previously results in a jet-black pellet, a dramatic color change from the unreacted starting materials.

The black color was maintained upon grinding. The FD resulted in loose powder similarly displaying a black coloration. When handling these materials side by side, the FD was fluffy and light, as opposed to the denser Conv. material.

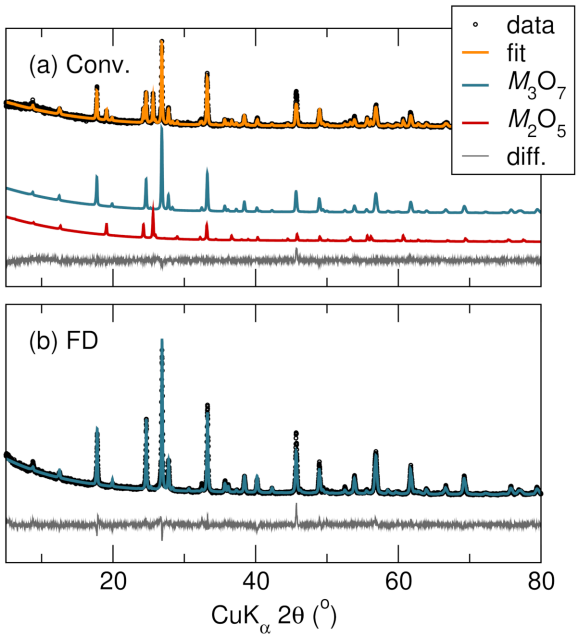

Figure 2: X-ray powder diffraction data for (a) the conventionally prepared material (labelled Conv.) and (b) the material prepared through the solution freeze-drying route (labelled FD), with the corresponding Rietveld fits to the appropriate crystal structure(s). The material made through the conventional route was refined to be 91 % of the target 3×3 block structure with the general formula M_3O_7 and 9 % the 4×4 block structure compound with the M_2O_5 formula in the same space group. The FD sample in (b) is single phase of the target 3×3 block structure. Refinement statistics can be found in the SI.

The structures were characterized with powder X-ray diffraction as shown in figure 2. Refinement statistics for both materials are included in the SI. After the first report of the $(W_{0.2}V_{0.8})_3O_7$ structure by Galy in 1964, solved from a single crystal, difficulties in the preparation of pure powders of the material have been reported.[27] After extensive optimization, the target crystal structure in the I4/mmm space group could be obtained, containing 9 % of 4×4 Wadsley block defects. These defects are well established in the literature and commonly occur where some of the blocks have a different size than the main structure.[68,69] The 4×4 block unit cell is presented in the SI. Because the fundamental structure and chemistry is unchanged with the small inclusion of the block defects, the

analyses will not be significantly impacted. Particles obtained from the FD route yielded a single phase corresponding to the 3×3 structure as seen in figure 2(b). This phase pure sample was possible for a number of reasons, most notably, mixing stoichiometric solutions of aqueous precursors allows for mixing on the atomic scale, as opposed to mixing on micron-sized length scales associated with reactions between bulk oxide powders. It is additionally important to note that lyophilizing the solution provided a much finer control of the stoichiometry, due in part to the poor solubility of the V precursor. Flash-freezing prevents the precipitation of V that would otherwise occur due to poor solubility in water. Besides agreeing well with the single crystal structure of Galy[45], XPS survey scans and energy-dispersive x-ray spectroscopy measurements (figures presented in the SI) showed very close agreement of the measured V:W ratio to the expected ratio of 4:1.

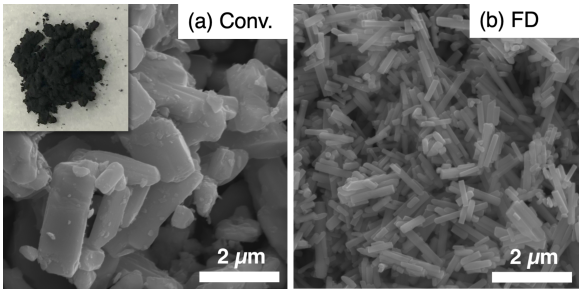

Figure 3: Scanning electron micrographs: (a) the conventionally prepared material (Conv.) displaying multiple-micron sized particles and (b) material prepared through the freeze-drying route (FD), displaying narrow lath-shaped particles up to a few microns in length but under 100 nm in width. A higher magnification image of the FD material can be found in the SI. The inset in (a) is a photograph of the as-prepared Conv. material showing the color associated with a partially filled d band.

Because solution-based methods provide diffusion pathways on the atomic scale, the FD preparation method allows for much shorter heating times compared to the Conv. preparation. Short calcination times equate to smaller particles seen in figure 3 where scanning electron microscopy reveals the Conv. particles to have a short rod-like morphology on the order of 1 μm to 2 μm in the shortest direction. The inset of figure 3(a) shows the resulting jet-black powder upon grinding the pellet. Figure 3(b) shows how the FD preparation resulted in much smaller, rod-like particles about 100 nm in the shortest direction. A higher

magnification of the FD particles is shown in the SI. The rod-like morphology is consistent with earlier transmission electron microscopy work on these compounds.[68]

Electrochemical lithiation revealed very comparable cycling between the Conv. and FD particles, and therefore the majority of the electrochemistry presented here focuses on the FD material. Additional electrochemistry of the Conv. material is included in the SI. At a C/5 rate on first discharge, more than 1 Li/TM is inserted. The impressive capacity retention by both large and small particles points to the crystal structure of $(W_{0.2}V_{0.8})_3O_7$ being conducive to the mobility of lithium.

Cyclic voltammetry was performed at different rates to determine an optimum voltage window for the electrochemistry, in addition to understanding the evolution of the redox peaks at varying sweep rates [Figure 4 (a)]. To avoid anomalous capacity contributions from lithium storage in carbon and electrolyte decomposition, a lower cutoff voltage of 1 V was selected.[70] Cyclic voltammetry reveals two major peaks on both reduction and oxidation. There is minimal redox activity until 2.4 V, where the first peak occurs, followed by an additional redox peak at 2 V. We note that the cyclic voltammetry reveals a significant amount of charge stored at potentials above 2 V, which differentiates this material from other, usually niobium-containing shear structures in the same family that typically store the majority of charge below 2 V.

Galvanostatic cycling at a 5C rate displayed in figure 4 (b) shows that after the first cycle, features of the discharge/charge curves are highly reproducible, with some capacity loss after the first cycle. The structure of the discharge curve displays three main regions, related to the trends we see in the cyclic voltammetry. At first, there is a steep voltage drop to 2.4 V where a small amount (0.25 Li) of lithium is incorporated into the structure. This leads to a small plateau that extends as a moderately sloping region until 2 V where 2.25 Li is inserted. Both of these redox events are consistent with the voltages observed from the cyclic voltammetry. The slope angles downward at this point until the 1 V cutoff where an additional 0.5 Li is incorporated. We observe moderate polarization between the

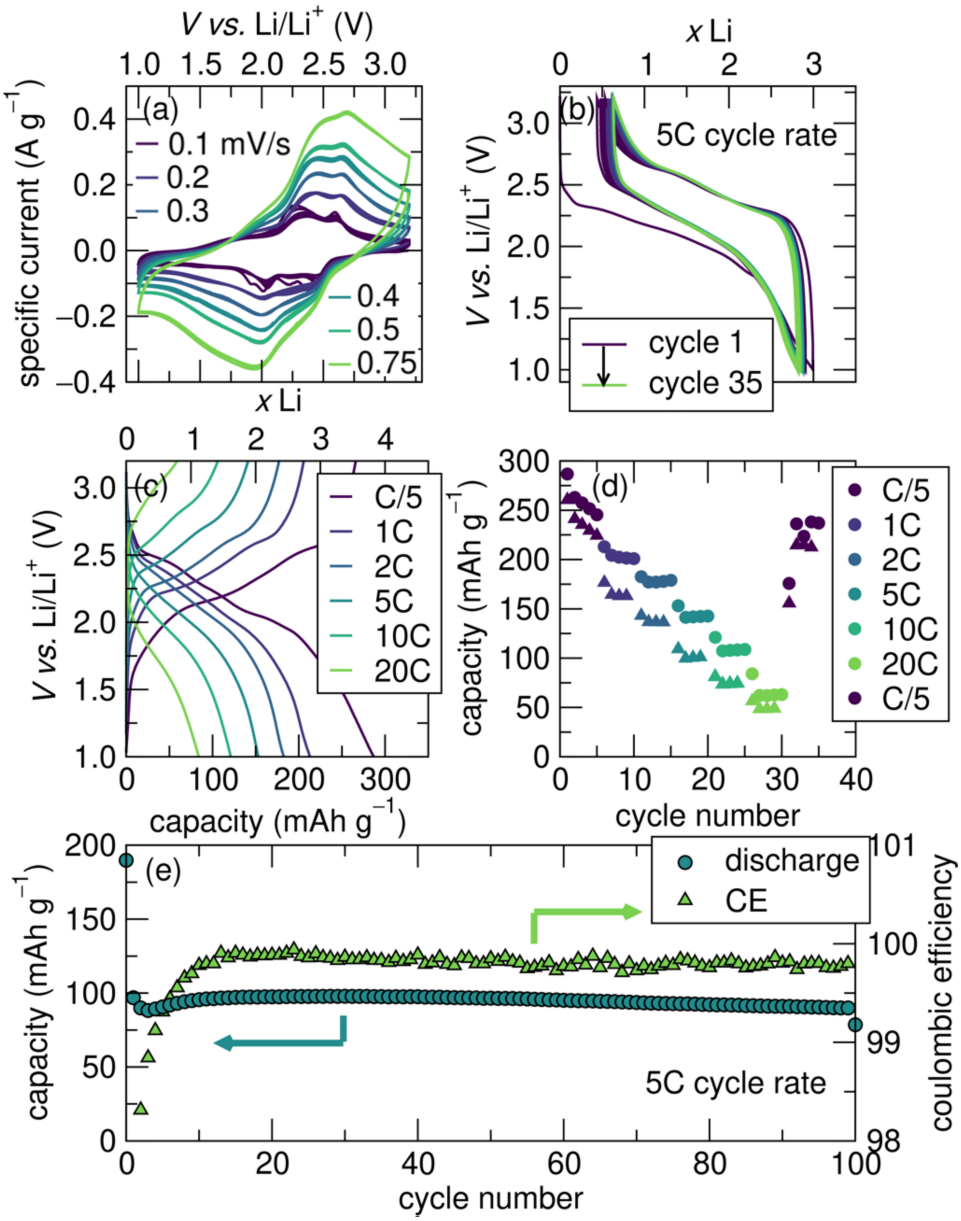

Figure 4: Electrochemistry of the FD $(W_{0.2}V_{0.8})_3O_7$ sample. (a) Variable rate cyclic voltammetry performed at sweep rates from 0.10 mV s^{-1} to 0.75 mV s^{-1}. (b) Galvanostatic cycling at a 5C rate shows slight irreversible capacity loss after the first cycle and moderate polarization. (c) Galvanostatic cycling at rates from C/5 to 20C, and its recovery. (d) Summary of rate performance during discharge as a function of cycle number from data depicted in (c). Circles represent the FD material and triangles representing the Conv. material are displayed to compare rate performance between the different sizes of particles. (e) Extended cycling at a 5C rate. The FD material shows high capacity retention and Coulombic efficiency over 100 cycles.

discharge and charge curves.

The material exhibits impressive rate capabilities, demonstrated in figure 4 (c). At the slowest C/5 rate, we observe the three regions of the discharge/charge curves described earlier. As the cycling rate is increased to 20C, the discharge curve becomes smooth and sloping, and the bulk of the capacity is instead stored below 2 V, as opposed to the slower rates where more charge is stored above 2 V. Figure 4(d) compares the variable rate galvanostatic cycling of the small particles to the micron-sized particles. Upon returning to slow rates after more rapid cycling, both materials recover most of the capacity observed at the beginning of cycling. The large Conv. particles show a comparable charge storage capacity at low and high rates, while the FD material shows the largest kinetic advantage at intermediate rates. As seen in figure 4 (e), $(W_{0.2}V_{0.8})_3O_7$ retains stable capacity at a 5C rate over 100 cycles.

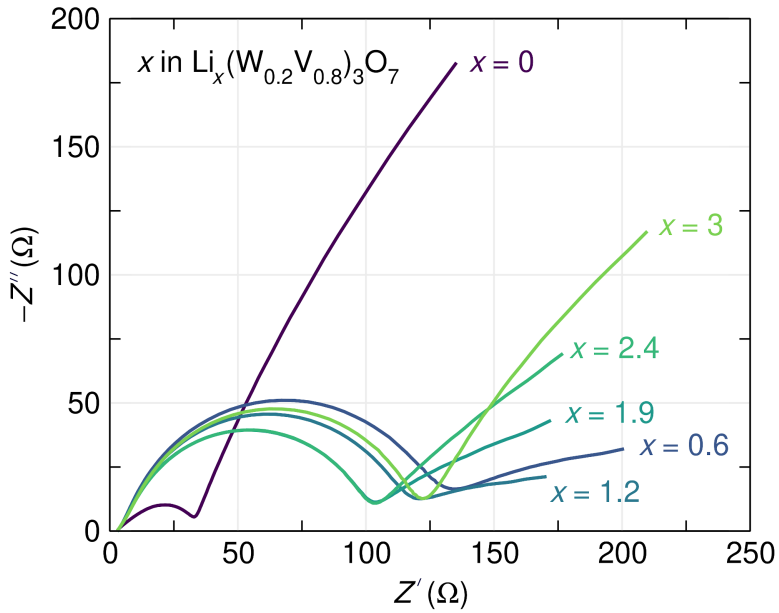

Figure 5: Electrochemical impedance spectra of $(W_{0.2}V_{0.8})_3O_7$ slurry electrodes as a function of Li content. The charge transfer resistance increases upon initial insertion of Li^+ but otherwise remains relatively constant at stoichiometries between $x = 0.6$ and $x = 3$ in $Li_x(W_{0.2}V_{0.8})_3O_7$. The spectra were collected on an electrode that had been previously cycled through galvanostatic rate testing so that initial SEI formation does not affect the data.

Highly electrically conducting electrodes, or ones that turn into electrical conductors

upon lithiation have the advantage of permitting fast cycling. Evidence for the effective electrical conductivity of $(W_{0.2}V_{0.8})_3O_7$ is seen from electrochemical impedance on the full cell. Potentiostatic electrochemical impedance spectroscopy was used to measure the charge transfer resistance of FD $(W_{0.2}V_{0.8})_3O_7$ slurry electrodes at different stages of lithiation (figure 5). The initial insertion of 0.6 Li^+ per unit cell results in an increase in the charge transfer resistance from about 30 Ω to 130 Ω. Additional lithiation results only in minor changes, and the electrode maintains a moderate charge transfer resistance of 100 Ω to 130 Ω up to insertion of 3 Li^+ per unit cell. These data suggest that the electrical resistivity of $(W_{0.2}V_{0.8})_3O_7$ remains reasonably low across the full range of electrochemical cycling.

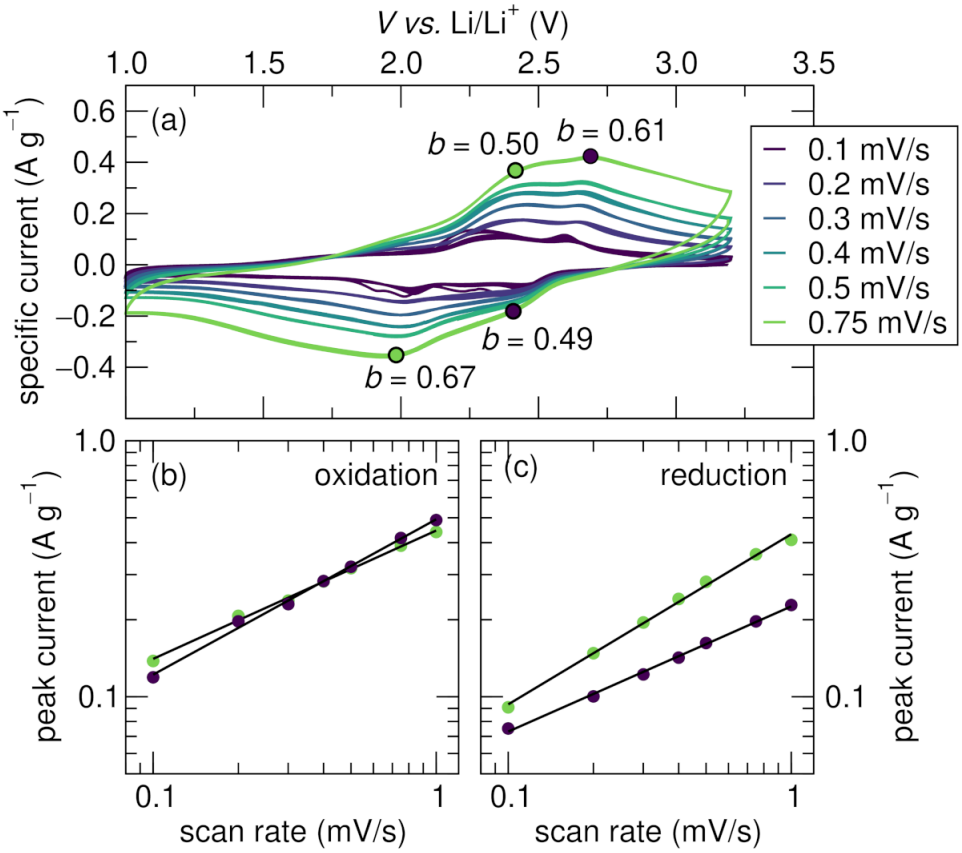

Figure 6: (a) Cyclic voltammetry of FD material at varying sweep rates, used to obtain the exponent b for the different peaks in the voltammograms (indicated on the figure). (b) Power law fits for each oxidation peak based on the relationship between the scan rate and the current. (c) The corresponding fits for each reduction peak.

In order to understand the nature of Li insertion and de-insertion, a kinetic study was carried out using the established relationship between the peak currents, I_p, in cyclic voltammetry to the voltage scan rate, v, through the power law: $I_p = av^b$, where a and b are constants. The exponent b extracted for each redox peak is then indicative of the underlying diffusion mechanism, with $b = 0.5$ corresponding to semi-infinite diffusion, and $b = 1.0$ corresponding to a non-diffusion controlled process.[34,71] $(W_{0.2}V_{0.8})_3O_7$ has two obvious redox peaks on both reduction and oxidation in the range of voltages scanned, as see in figure 6(a). By extracting the peak currents and fitting to the power law equation above, as demonstrated for the oxidation peaks in figure 6(b) and the reduction peaks in figure 6(c), the various values of the exponent b are obtained, which are presented against the respective redox peaks in figure 6(a). The values of b for all redox processes are close to 0.5, which indicates processes limited by bulk semi-infinite diffusion. This strongly points to the electrode materials storing charge though conventional electrochemical Li insertion rather than for example, capacitive storage taking place at the interface.

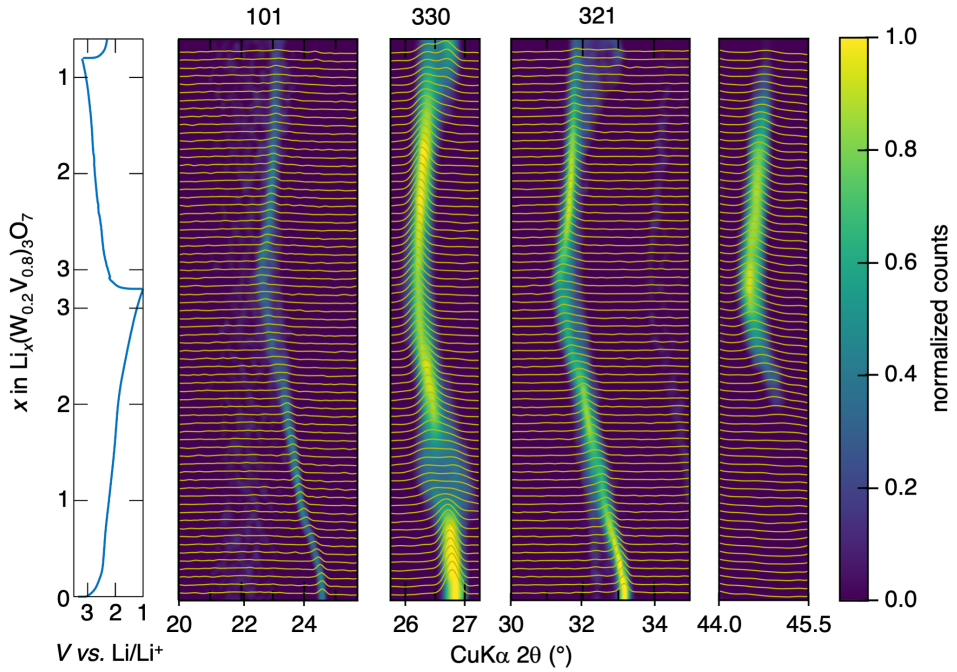

Figure 7: Select regions in the *operando* X-ray diffraction patterns of the FD $(W_{0.2}V_{0.8})_3O_7$ material during the first galvanostatic cycle at a rate of C/10. The corresponding electrochemistry is shown on the left most panel.

Operando X-ray powder diffraction of $(W_{0.2}V_{0.8})_3O_7$ performed at a C/10 rate provides insightful information about the evolution of the structure during lithium insertion and extraction. Select diffraction peaks during cycling are displayed in panels in figure 7. Data collected over the full 2θ range is presented in the SI, along with a summary of the Rietveld refinements during lithiation. $(W_{0.2}V_{0.8})_3O_7$ appears to display mostly solid solution behavior. At the start of Li insertion and up to 1 Li/formula unit, a slight expansion of the unit cell is observed in the presented reflections. After this point, the (330) peak splits in the composition range between 1 Li per formula to 2 Li per formula. The peak splitting is attributed to the existence of a narrow two-phase region that then disappears above 2 Li per formula and then reappears on the following discharge cycle. Shortly after the disappearance of the peak splitting at (330), a new diffraction peak emerges at $2\theta \approx 45^\circ$. Along with the (110), (330), and (321) peaks that are tracked, this new peak similarly indicates unit cell expansion with increasing lithiation, followed by contraction as Li is removed. This feature indicates a phase change that disappears at the end of charge. At full discharge, the a and b planes expand by only 2.5 % while the c plane expands by 6.4 %. We see an overall volume expansion of 13 %, in good agreement with previous chemical insertion on related compound $W_{0.2}V_{2.8}O_7$.[28] The refinements of the lithiated material are summarized in the SI as is the evolution of the cell parameters and cell volume with lithiation. The observed expansion on the basis of the number of electrons per transition element is relatively large compared with what has been observed in related Nb-rich oxides. This may in part help understanding why the high-rate cycling of $(W_{0.2}V_{0.8})_3O_7$ results in reduced storage capacity compared with compounds in the structurally related the Nb–W–O series.[37]

The structural evolution of this material seen through *operando* powder diffraction explicitly shows how $(W_{0.2}V_{0.8})_3O_7$ behaves as a battery material, in agreement with the analysis of the exponent b in the variable-rate cyclic voltammetry. In the parent ReO_3 structure, Li conduction through the three-dimensional octahedral network is hampered

due to rotation and tilting of the solely corner-connected octahedra. When there are edge-sharing features associated with crystallographic shear, rotation and tilting are prevented and Li transport is not impeded.[42,72] However, the channels in the structure created by octahedral corner-sharing create highways for Li diffusion.

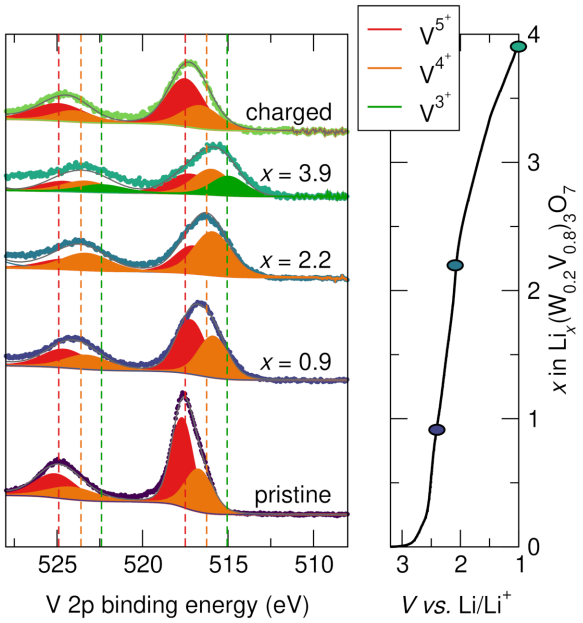

Figure 8: X-ray photoelectron spectra displaying the region of V $2p$ spin-orbit doublets $2p_{3/2}$ and $2p_{1/2}$ for the Conv. material. The total fit and contributions from the different oxidation states are indicated. On the right is the first galvanostatic discharge for Li insertion with the points indicating where the ex-situ XPS spectra were acquired.

Both constituent transition metals are capable of multielectron redox, with a maximum theoretical capacity of 342 mAh g^{-1} if 4.4 e^{-1} are inserted (where we assume W^{6+} reduces to W^{4+}, V^{4+} reduces to V^{3+}, and V^{5+} reduces to V^{3+}), based off initial oxidation states of the transition metals according to the equation $(1-y)V_2O_5$ $+(1+y)VO_2$ $+$ yWO_3 $\rightarrow$ $W_yV_{3-y}O_7$. Although this level of lithiation is not observed experimentally in the voltage ranges employed, the electrochemistry shows that 1.3 Li^+/TM are inserted at a C/5 rate, indicating that at least one of the transition metals is participating in a multielectron redox process. Ex-situ XPS allows this to be understood, however is not quantitatively relatable to the bulk oxidation states because of surface sensitivity to oxidation. Figure 8(b) and figure 9(b) display spectra at different states of charge for V and W respectively in the

Conv. material. The pristine material appears to be a combination of V^{5+} and V^{4+} but only W^{6+}. As 0.9 Li inserts into the structure, further reduction of the V^{5+} species to V^{4+} is observed. After 2.2 Li inserts, the proportion of V^{5+} to V^{4+} inverts and the majority of V states are V^{4+}. At full discharge with insertion of 3.9 Li, 27 % of the V is reduced to V^{3+}. Upon charge, the V oxidizes back to V^{5+} and V^{4+}, but with a slightly higher ratio of V^{4+} than observed in the pristine material. This could be attributed to part of the irreversible capacity loss seen after the first cycle.

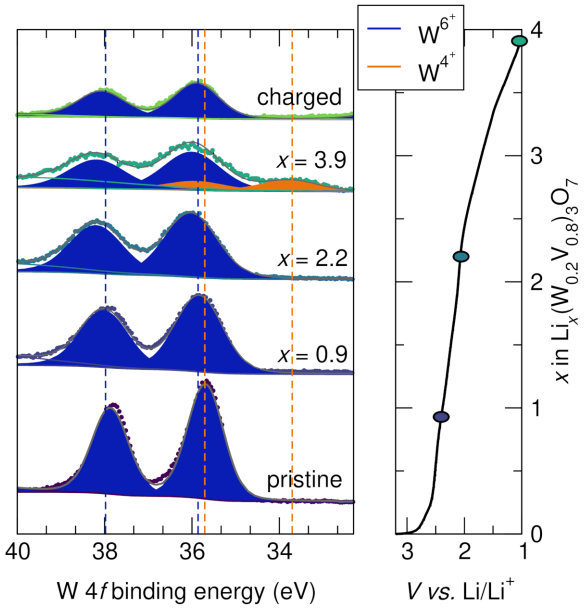

Figure 9: (left) X-ray photoelectron spectra of the W $4f$ binding energy region displaying the lower-energy W $4f_{7/2}$ and higher binding energy W $4f_{5/2}$ spin-orbit doublets. The grey line on each spectrum shows the total fit that combines the fits from each of the individual oxidation states. (right) First galvanostatic discharge for Li insertion into Conv. $(W_{0.2}V_{0.8})_3O_7$ material. States of charge corresponding to XPS spectra are overlaid on discharge curve.

In contrast to V, W reduction is quite different. W remains in its W^{6+} oxidation state almost until full discharge where 23 % of the W is reduced to W^{4+}. There appears to be no evidence in the XPS signatures for any intermediate W^{5+} state[73] which could suggest a tendency to valence-skip in this structure type. W returns to being fully oxidized after charging. These results confirm multielectron redox in both of the transition metals. As confirmed with XPS, the pristine $(W_{0.2}V_{0.8})_3O_7$ begins in a non-d^0 state due to a fraction

of partially reduced V [figure 8 (b)]. This is what results in the compound, even prior to lithiation, displaying some evidence of electrical conduction and being black in color.

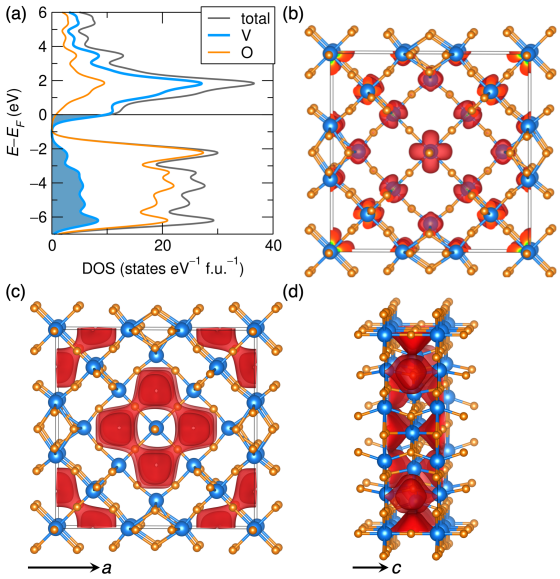

Figure 10: (a) Density of states for model compound V_3O_7 showing contributions from filled vanadium states at the Fermi level. (b) Charge density isosurface level of 0.005 e Å^{-3} depicted within the unit cell of V_3O_7 showing the 1 d electron in the formula prefers the middle of the 3×3 block. (c) and (d) View of the bond valence difference map for Li in the space of the structure of V_3O_7 displayed for an isosurface value Δv =0.1 valence units.

As discussed above, although the samples were transferred from the glovebox using an air-free sample holder, some surface oxidation can occur which skews measurements towards higher oxidation states. This means that we cannot expect the XPS to quantitatively reflect the bulk oxidation state, but it should still be an excellent indication of the redox states present in the material as a function of Li content.

Density-functional theory-based electronic structure calculations are employed to provide qualitative understanding these 3×3 block structured materials as Li hosts. A complete analysis of the electronic structure of the parent $(W_{0.2}V_{0.8})_3O_7$ compound must account for the combination of electron correlation and disorder (the latter enhancing the former) which is beyond the scope of this work. However, calculations on the isostructural model compound V_3O_7 provide some useful insights. From the densities of state displayed for V_3O_7 figure 10(a), we see a combination of oxygen, but primarily transition metal states

at the Fermi energy, arising from the formally, 1 d electron for every three V, which is also consistent with what is observed in the XPS of the starting $(W_{0.2}V_{0.8})_3O_7$ compound. The as-calculated structure does not stabilize magnetization, even with the DFT simulations performed using the SCAN functional, which usually enhances magnetic localization. The partial charge density in figure 10(b) corresponds to a visualization of states in the energy range around E_F. The data suggests that the electron prefers the central metal site on an octahedron that is purely corner-sharing. This has also been noted in other shear phases, for example in $Li_xPNb_9O_{25}$ where the initial doped electrons localize (albeit magnetically in that case) on the central corner-connected octahedron.[40] As stated above, W/V substitution is likely to further hinder electron transport due to disorder and potentially yield some local moment behavior in the magnetism.

Bond valence mapping provides a simple means of estimating ion transport pathways and mechanisms for mobile ions placed arbitrarily within a 3D crystal structure. For each location in the 3D space of the structure, the absolute value of the difference Δv between the valence calculated for the probe ion (here Li^+) at that site and its actual electrostatic valence (1 for Li^+) is mapped.[74,75] It is possible to relate this valence difference Δv to energies of defect formation and defect migration, allowing for rough predictions of the activation energy required for ion transport.[74,75] Isosurfaces for a value of Δv=0.1 in valence units for the model compound V_3O_7 are displayed in panels (c) and (d) of figure 10. This isosurface illustrates probable 3D lithium migration paths in the structure. Empirically, it has been noted that the activation energy in eV is equivalent to approximately $2\times\Delta v$ in units,[76] so the displayed isosurface, forming channels down the c axis of the structure, indeed suggests a low energy pathway for Li^+ migration. This is consistent with other, prior work showing in related shear structures that ion conduction occurs most rapidly in the center of the blocks in related shear structures.[77] ReO_3 has itself been shown to display an activation energy of migration for Li^+ of 0.1 eV,[78] which is in line with the values presented here. More detailed DFT studies to complement experimental investigations by impedance

spectroscopy and NMR are necessary to establish the complete picture.[79]

Conclusion

Electrochemical insertion studies of $(W_{0.2}V_{0.8})_3O_7$ show that this vanadium-rich shear-structured Wadsley–Roth phase is a promising high-rate electrode material. While both the larger conventionally synthesized particles and smaller particles obtained by solution freeze-drying and calcination have capacity retention at up to 20C, there appears to be a clear advantage at all rates in having smaller particles. Distinct from other, mostly niobium-containing shear structured compounds, the pristine material is a black powder that begins with some finite d state population and therefore could be an intrinsically better electrical conductor than comparable d^0 oxides. Multielectron redox of both W and V lead to high specific capacities, while slight and reversible structural changes allow for capacity retention over one hundred cycles. This compound stores more charge at higher voltages than most other reported Wadsley–Roth compounds and points to promising directions for tuning the voltage in this high-performance class of electrode materials.

Supporting Information

The Supporting Information is available free of charge at [] with further details of the crystal structures, electrochemistry, diffraction and XPS.

Acknowledgement

This work was supported as part of the Center for Synthetic Control Across Length scales for Advancing Rechargeables (SCALAR), an Energy Frontier Research Center funded by the U.S. Department of Energy, Office of Science, Basic Energy Sciences under Award DE-

SC0019381. The research reported here made use of shared facilities of the UC Santa Barbara Materials Research Science and Engineering Center (MRSEC, NSF DMR 1720256), a member of the Materials Research Facilities Network (www.mrfn.org). We acknowledge use of the shared computing facilities of the Center for Scientific Computing at UC Santa Barbara, supported by NSF CNS-1725797, and the NSF MRSEC at UC Santa Barbara, NSF DMR-1720256. D.R. has been supported by the National Science Foundation Graduate Research Fellowship Program under Grants DGE-1650604 and DGE-2034835. S.M.L.T. has been supported by the National Science Foundation Graduate Research Fellowship Program under Grant DGE-1650114. Any opinions, findings, and conclusions or recommendations expressed in this material are those of the authors and do not necessarily reflect the views of the National Science Foundation. It is a pleasure to thank Miguel Zepeda of the UC Santa Barbara Materials Research Laboratory for help with *operando* XRD.

References

(1) Dunn, B.; Kamath, H.; Tarascon, J.-M. Electrical Energy Storage for the Grid: A Battery of Choices. *Science* **2011**, *334*, 928–935.

(2) Lukatskaya, M. R.; Dunn, B.; Gogotsi, Y. Multidimensional materials and device architectures for future hybrid energy storage. *Nat. Commun.* **2016**, *7*, 12647.

(3) Goodenough, J. B.; Park, K. S. The Li-Ion Rechargeable Battery: A Perspective. *J. Am. Chem. Soc.* **2013**, *135*, 1167–1176.

(4) Wang, Y.; Cao, G. Developments in Nanostructured Cathode Materials for High-Performance Lithium-Ion Batteries. *Adv. Mater.* **2008**, *20*, 2251–2269.

(5) Mukherjee, R.; Krishnan, R.; Lu, T.-M.; Koratkar, N. Nanostructured Electrodes for High-Power Lithium Ion Batteries. *Nano Energy* **2012**, *1*, 518–533.

(6) Kim, D.-H.; Kim, J. Synthesis of $LiFePO_4$ Nanoparticles in Polyol Medium and Their Electrochemical Properties. *Electrochem. Solid-State Lett.* **2006**, *9*, A439–A442.

(7) Yang, Z.; Choi, D.; Kerisit, S.; Rosso, K. M.; Wang, D.; Zhang, J.; Graff, G.; Liu, J. Nanostructures and lithium electrochemical reactivity of lithium titanites and titanium oxides: A review. *J. Power Sources* **2009**, *192*, 588–598.

(8) Palacín, M. R.; Simon, P.; Tarascon, J. M. Nanomaterials for Electrochemical Energy Storage: The Good and the Bad. *Acta Chim. Slov.* **2016**, *63*, 417–423.

(9) Cook, J. B.; Lin, T. C.; Kim, H.-S.; Siordia, A.; Dunn, B. S.; Tolbert, S. H. Suppression of Electrochemically Driven Phase Transitions in Nanostructured MoS_2 Pseudocapacitors Probed Using *Operando* X-ray Diffraction. *ACS Nano* **2019**, *13*, 1223–1231.

(10) Doeff, M. M.; Wilcox, J. D.; Kostecki, R.; Lau, G. Optimization of Carbon Coatings on $LiFePO_4$. *J. Power Sources* **2006**, *163*, 180–184.

(11) Shin, H. C.; Cho, W. I.; Jang, H. Electrochemical Properties of Carbon-Coated $LiFePO_4$ Cathode Using Graphite, Carbon Black, and acetylene black. *Electrochim. Acta* **2006**, *52*, 1472–1476.

(12) Jiang, J.; Dahn, J. R. Dependence of the Heat of Reaction of $Li_{0.81}C_6$ (0.1 V), $Li_7Ti_5O_{12}$ (1.55 V), and $Li_{0.5}VO_2$ (2.45 V) Reacting with Nonaqueous Solvents or Electrolytes on the Average Potential of the Electrode Material. *J. Electrochem. Soc.* **2006**, *153*, A310–A315.

(13) Downie, L. E.; Krause, L. J.; Burns, J. C.; Jensen, L. D.; Chevrier, V. L.; Dahn, J. R. In Situ Detection of Lithium Plating on Graphite Electrodes by Electrochemical Calorimetry. *J. Electrochem. Soc.* **2013**, *160*, A588–A594.

(14) Burns, J. C.; Stevens, D. A.; Dahn, J. R. In-Situ Detection of Lithium Plating Using High Precision Coulometry. *J. Electrochem. Soc.* **2015**, *162*, A959–A964.

(15) Ribière, P.; Grugeon, S.; Morcrette, M.; Boyanov, S.; Laruelle, S.; Marlair, G. Investigation on the fire-induced hazards of Li-ion battery cells by fire calorimetry. *Energy Environ. Sci.* **2012**, *5*, 5271–5280.

(16) Zhao, K.; Pharr, M.; Vlassak, J. J.; Suo, Z. Fracture of Electrodes in Lithium-Ion Batteries Caused by Fast Charging. *J. Appl. Phys.* **2010**, *108*, 073517.

(17) Odziomek, M.; Chaput, F.; Rutkowska, A.; Świerczek, K.; Olszewska, D.; Sitarz, M.; Lerouge, F.; Parola, S. Hierarchically Structured Lithium Titanate for Ultrafast Charging in Long-Life High Capacity Batteries. *Nat. Commun.* **2017**, *8*, 15636.

(18) Hayner, C. M.; Zhao, X.; Kung, H. H. Materials for Rechargeable Lithium-Ion Batteries. *Annu. Rev. Chem. Biomol. Eng.* **2012**, *3*, 445–471.

(19) Magnéli, A. The Crystal Structures of Mo_90_{26} (β'-Molybdenum Oxide) and Mo_80_{23} (β-Molybdenum Oxide). *Acta Chem. Scand.* **1948**, *8*, 501–517.

(20) Roth, R.; Wadsley, A. Multiple Phase Formation in the Binary system Nb_2O_5–WO_3. I. Preparation and Identification of Phases. *Acta Crystallogr.* **1965**, *19*, 26–32.

(21) Roth, R.; Wadsley, A.; Andersson, S. The Crystal Structure of PNb_9O_{25}, ($P_2O_5 \cdot 9Nb_2O_5$). *Acta Crystallogr.* **1965**, *18*, 643–647.

(22) Andersson, S.; Wadsley, A. D. Crystallographic Shear and Diffusion Paths in Certain Higher Oxides of Niobium, Tungsten, Molybdenum and Titanium. *Nature* **1966**, *211*, 581–583.

(23) Andersson, S. The description of non-stoichiometric transition metal oxides. A logical extension of inorganic crystallography. *Bull. Mineral.* **1967**, *90*, 522–527.

(24) Cheetham, A.; Von Dreele, R. Cation Distributions in Niobium Oxide Block Structures. *Nat. Phys. Sci.* **1973**, *244*, 139–140.

(25) Dreele, R. V.; Cheetham, A. K. The structures of some titanium-niobium oxides by powder neutron diffraction. *Proc. R. Soc. Lond. A* **1974**, *338*, 311–326.

(26) Murphy, D.; Greenblatt, M.; Cava, R. J.; Zahurak, S. Topotactic Lithium Reactions with ReO_3 Related Shear Structures. *Solid State Ionics* **1981**, *5*, 327–329.

(27) Cava, R. J.; Kleinman, D. J.; Zahurak, S. M. $V_{3.2}W_{1.8}O_{13}$ and Studies of the V_2O_5–WO_3–VO_2 Ternary System. *Mater. Res. Bull.* **1983**, *18*, 869–873.

(28) Cava, R. J.; Murphy, D. W.; Zahurak, S. M. Lithium Insertion in Wadsley-Roth Phases Based on Niobium Oxide. *J. Electrochem. Soc.* **1983**, *130*, 2345–2351.

(29) Cava, R. J.; Santoro, A.; Murphy, D. W.; Zahurak, S. M.; Roth, R. S. The Structures of the Lithium Inserted Metal Oxides $Li_{0.2}ReO_3$ and $Li_{0.36}WO_3$. *J. Solid State Chem.* **1983**, *50*, 121–128.

(30) Cava, R. J.; Murphy, D.; Rietman, E.; Zahurak, S.; Barz, H. Lithium Insertion, Electrical Conductivity, and Chemical Substitution in Various Crystallographic Shear Structures. *Solid State Ionics* **1983**, *9*, 407–411.

(31) Han, J. T.; Huang, Y. H.; Goodenough, J. B. New Anode Framework for Rechargeable Lithium Batteries. *Chem. Mater.* **2011**, *23*, 2027–2029.

(32) Han, J.-T.; Goodenough, J. B. 3-V Full Cell Performance of Anode Framework $TiNb_2O_7$/Spinel $LiNi_{0.5}Mn_{1.5}O_4$. *Chem. Mater.* **2011**, *23*, 3404–3407.

(33) Saritha, D.; Pralong, V.; Varadaraju, U. V.; Raveau, B. Electrochemical Li Insertion Studies on $WNb_{12}O_{33}$ – A Shear ReO_3 Type Structure. *J. Solid State Chem.* **2010**, *183*, 988–993.

(34) Augustyn, V.; Come, J.; Lowe, M. A.; Kim, J. W.; Taberna, P. L.; Tolbert, S. H.; Abruña, H. D.; Simon, P.; Dunn, B. High-rate electrochemical energy storage through Li^+ intercalation pseudocapacitance. *Nat. Mater.* **2013**, *12*, 518–522.

(35) Griffith, K. J.; Forse, A. C.; Griffin, J. M.; Grey, C. P. High-Rate Intercalation without Nanostructuring in Metastable Nb_2O_5 Bronze Phases. *J. Am. Chem. Soc.* **2016**, *138*, 8888–8899.

(36) Griffith, K. J.; Senyshyn, A.; Grey, C. P. Structural Stability from Crystallographic Shear in TiO_2-Nb_2O_5 Phases: Cation Ordering and Lithiation Behavior of $TiNb_{24}O_{62}$. *Inorg. Chem.* **2017**, *56*, 4002–4010.

(37) Griffith, K. J.; Wiaderek, K. M.; Cibin, G.; Marbella, L. E.; Grey, C. P. Niobium tungsten oxides for high-rate lithium-ion energy storage. *Nature* **2018**, *559*, 556–563.

(38) Griffith, K. J.; Seymour, I. D.; Hope, M. A.; Butala, M. M.; Lamontagne, L. K.; Preefer, M. B.; Koçer, C. P.; Henkelman, G.; Morris, A. J.; Cliffe, M. J.; Dutton, S. E.;

Grey, C. P. Ionic and Electronic Conduction in $TiNb_2O_7$. *J. Am. Chem. Soc.* **2019**, *141*, 16706–16725.

(39) Zhu, X.; Xu, J.; Luo, Y.; Fu, Q.; Liang, G.; Luo, L.; Chen, Y.; Lin, C.; Zhao, X. $MoNb_{12}O_{33}$ as a new anode material for high-capacity, safe, rapid and durable Li^+ Storage: structural characteristics, electrochemical properties and working mechanisms. *J. Mater. Chem. A* **2019**, *7*, 6522–6532.

(40) Preefer, M. B.; Saber, M.; Wei, Q.; Bashian, N. H.; Bocarsly, J. D.; Zhang, W.; Lee, G.; Milam-Guerrero, J.; Howard, E. S.; Vincent, R. C.; Melot, B. C.; Van der Ven, A.; Seshadri, R.; Dunn, B. S. Multielectron Redox and Insulator-to-Metal Transition upon Lithium Insertion in the Fast-Charging, Wadsley-Roth Phase PNb_9O_{25}. *Chem. Mater.* **2020**, *32*, 4553–4563.

(41) Koçer, C. P.; Griffith, K. J.; Grey, C. P.; Morris, A. J. Cation Disorder and Lithium Insertion Mechanism of Wadsley-Roth Crystallographic Shear Phases from First Principles. *J. Am. Chem. Soc.* **2019**, *141*, 15121–15134.

(42) Bashian, N. H.; Zhou, S.; Zuba, M.; Ganose, A. M.; Stiles, J. W.; Ee, A.; Ashby, D. S.; Scanlon, D. O.; Piper, L. F.; Dunn, B.; Melot, B. C. Correlated Polyhedral Rotations in the Absence of Polarons during Electrochemical Insertion of Lithium in ReO_3. *ACS Energy Lett.* **2018**, *3*, 2513–2519.

(43) Griffith, K. J.; Grey, C. P. Superionic Lithium Intercalation through 2×2 nm^2 Columns in the Crystallographic Shear Phase $Nb_{18}W_8O_{69}$. *Chem. Mater.* **2020**, *32*, 3860–3868.

(44) Gaultois, M. W.; Sparks, T. D.; Borg, C. K.; Seshadri, R.; Bonificio, W. D.; Clarke, D. R. Data-Driven Review of Thermoelectric Materials: Performance and Resource Considerations. *Chem. Mater.* **2013**, *25*, 2911–2920.

(45) Darriet, J.; Galy, J. $(W_{0.2}V_{0.8})_3O_7$: Synthese et Structure Cristalline. *J. Solid State Chem.* **1972**, *4*, 357–361.

(46) Zibrov, I.; Filonenko, V.; Sidorov, V.; Lyapin, S. $V_{3.047}O_7$, a New High-Pressure Oxide with the Simpsonite Structure. *Inorg. Mater.* **2016**, *52*, 902–908.

(47) Voskanyan, A. A.; Abramchuk, M.; Navrotsky, A. Entropy Stabilization of TiO_2–Nb_2O_5 Wadsley–Roth Shear Phases and Their Prospects for Lithium-Ion Battery Anode Materials. *Chem. Mater.* **2020**, *32*, 5301–5308.

(48) Coelho, A. A. *TOPAS* and *TOPAS-Academic*: An Optimization Program Integrating Computer Algebra and Crystallographic Objects Written in C++. *J. Appl. Crystallogr.* **2018**, *51*, 210–218.

(49) Momma, K.; Izumi, F. *VESTA 3* For Three-Dimensional Visualization of Crystal, Volumetric and Morphology Data. *J. Appl. Crystallogr.* **2011**, *44*, 1272–1276.

(50) Stickel, J. J. Data Smoothing and Numerical Differentiation by a Regularization Method. *Comput. Chem. Eng.* **2010**, *34*, 467–475.

(51) Dedryvère, R.; Martinez, H.; Leroy, S.; Lemordant, D.; Bonhomme, F.; Biensan, P.; Gonbeau, D. Surface Film Formation on Electrodes in a $LiCoO_2$/Graphite cell: A Step by Step XPS Study. *J. Power Sources* **2007**, *174*, 462–468.

(52) Eshkenazi, V.; Peled, E.; Burstein, L.; Golodnitsky, D. XPS Analysis of the SEI Formed on Carbonaceous Materials. *Solid State Ionics* **2004**, *170*, 83–91.

(53) Verma, P.; Maire, P.; Novák, P. A Review of the Features and Analyses of the Solid Electrolyte Interphase in Li-ion Batteries. *Electrochim. Acta* **2010**, *55*, 6332–6341.

(54) Silversmit, G.; Depla, D.; Poelman, H.; Marin, G. B.; De Gryse, R. Determination of the V2p XPS Binding Energies for Different Vanadium Oxidation States (V^{5+} to V^{0+}). *J. Electron Spectrosc. Relat. Phenom.* **2004**, *135*, 167–175.

(55) Kresse, G.; Hafner, J. *Ab initio* Molecular-Dynamics Simulation of the Liquid-Metal–Amorphous-Semiconductor Transition in Germanium. *Phys. Rev. B* **1994**, *49*, 251–269.

(56) Kresse, G.; Furthmüller, J. Efficient Iterative Schemes for *ab initio* Total-Energy Calculations Using a Plane-Wave Basis Set. *Phys. Rev. B* **1996**, *54*, 169–186.

(57) Kresse, G.; Furthmüller, J. Efficiency of *Ab-Initio* Total Energy Calculations for Metals and Semiconductors Using a Plane-Wave Basis Set. *Comput. Mater. Sci.* **1996**, *6*, 15–50.

(58) Blöchl, P. E. Projector Augmented-Wave Method. *Phys. Rev. B* **1994**, *50*, 953–979.

(59) Kresse, G.; Joubert, D. From Ultrasoft Pseudopotentials to the Projector Augmented-Wave Method. *Phys. Rev. B* **1999**, *59*, 1758–1775.

(60) Perdew, J. P.; Burke, K.; Ernzerhof, M. Generalized Gradient Approximation Made Simple. *Phys. Rev. Lett.* **1996**, *77*, 3865–3868.

(61) Sun, J.; Ruzsinszky, A.; Perdew, J. P. Strongly Constrained and Appropriately Normed Semilocal Density Functional. *Phys. Rev. Lett.* **2015**, *115*, 1–6.

(62) Chakraborty, A.; Dixit, M.; Aurbach, D.; Major, D. T. Predicting Accurate Cathode properties of Layered Oxide Materials Using the SCAN Meta-GGA Density Functional. *npj Comput. Mater.* **2018**, *4*, 1–9.

(63) Dronskowski, R.; Bloechl, P. E. Crystal Orbital Hamilton Populations (COHP). Energy-Resolved Visualization of Chemical Bonding in Solids Based on Density-Functional Calculations. *J. Phys. Chem.* **1993**, *97*, 8617–8624.

(64) Deringer, V. L.; Tchougréeff, A. L.; Dronskowski, R. Crystal Orbital Hamilton Population (COHP) Analysis as Projected from Plane-Wave Basis Sets. *J. Phys. Chem. A* **2011**, *115*, 5461–5466.

(65) Maintz, S.; Deringer, V. L.; Tchougréeff, A. L.; Dronskowski, R. Analytic Projection From Plane-Wave and PAW Wavefunctions and Application to Chemical-Bonding Analysis in Solids. *J. Comput. Chem.* **2013**, *34*, 2557–2567.

(66) Maintz, S.; Deringer, V. L.; Tchougréeff, A. L.; Dronskowski, R. LOBSTER: A Tool to Extract Chemical Bonding from Plane-Wave Based DFT. *J. Comput. Chem.* **2016**, *37*, 1030–1035.

(67) Nishimura, S. PyAbstantia. 2017; `https://shinichinishimura.github.io/pyabst/`, (Accessed on October 11, 2019).

(68) Heurung, G.; Gruehn, R. High-Resolution Transmission Electron Microscopy – Investigation of Vanadium–Tungsten Oxides Prepared by Chemical Transport Reactions. *J. Solid State Chem.* **1984**, *55*, 337–343.

(69) Allpress, J.; Sanders, J.; Wadsley, A. Multiple Phase Formation in the Binary System Nb_2O_5–WO_3. VI. Electron Microscopic Observation and Evaluation of Non-Periodic Shear Structures. *Acta Crystallogr. B* **1969**, *25*, 1156–1164.

(70) See, K. A.; Lumley, M. A.; Stucky, G. D.; Grey, C. P.; Seshadri, R. Reversible Capacity of Conductive Carbon Additives at Low Potentials: Caveats for Testing Alternative Anode Materials for Li-Ion Batteries. *J. Electrochem. Soc.* **2017**, *164*, A327–A333.

(71) Augustyn, V.; Simon, P.; Dunn, B. Pseudocapacitive oxide materials for high-rate electrochemical energy storage. *Energy Environ. Sci.* **2014**, *7*, 1597–1614.

(72) Gopalakrishnan, J. Insertion/Extraction of Lithium and Sodium in Transition Metal Oxides and Chalcogenides. *Bull. Mater. Sci.* **1985**, *7*, 201–214.

(73) Xie, F.; Gong, L.; Liu, X.; Tao, Y.; Zhang, W.; Chen, S.; Meng, H.; Chen, J. XPS Studies on Surface Reduction of Tungsten Oxide Nanowire Film by Ar^+ Bombardment. *J. Electron Spectrosc. Relat. Phenom.* **2012**, *185*, 112–118.

(74) Adams, S. From Bond Valence Maps to Energy Landscapes for Mobile Ions in Ion-Conducting Solids. *Solid State Ionics* **2006**, *177*, 1625–1630.

(75) Adams, S.; Rao, R. P. High Power Lithium Ion Battery Materials by Computational Design. *Phys. Status Solidi A* **2011**, *208*, 1746–1753.

(76) Brown, I. D. Recent Developments in the Methods and Applications of the Bond Valence Model. *Chem. Rev.* **2009**, *109*, 6858–6919.

(77) Koçer, C. P.; Griffith, K. J.; Grey, C. P.; Morris, A. J. First-Principles Study of Localized and Delocalized Electronic States in Crystallographic Shear Phases of Niobium Oxide. *Phys. Rev. B* **2019**, *99*, 075151.

(78) Parras, J.; Genreith-Schriever, A.; Zhang, H.; Elm, M.; Norby, T.; De Souza, R. Is ReO_3 A mixed Ionic–Electronic conductor? A DFT Study of Defect Formation and Migration in a $B^{VI}O_3$ Perovskite-Type Oxide. *Phys. Chem. Chem. Phys.* **2018**, *20*, 8008–8015.

(79) Heins, T. P.; Harms, N.; Schramm, L.-S.; Schröder, U. Development of a New Electrochemical Impedance Spectroscopy Approach for Monitoring the Solid Electrolyte Interphase Formation. *Energy Technol.* **2016**, *4*, 1509–1513.

Graphical TOC Entry

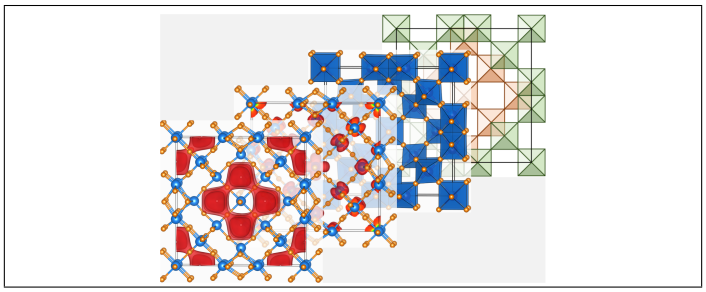

Supporting Information: High Capacity Li^+ Storage through Multielectron Redox in the Fast-Charging Wadsley–Roth Phase $(W_{0.2}V_{0.8})_3O_7$

Kira E. Wyckoff,[†,⊥] Daniel D. Robertson,[‡,⊥] Molleigh B. Preefer,[¶] Samuel M. L. Teicher,[†] Jadon Bienz,[¶] Linus Kautzsch,[†] Thomas E. Mates,[†] Joya A. Cooley,[§] Sarah H. Tolbert,[*,‡,∥] and Ram Seshadri[*,†,¶]

†*Materials Department and Materials Research Laboratory*
University of California, Santa Barbara, California 93106, United States
‡*Department of Chemistry and Biochemistry*
University of California, Los Angeles, California 90095, United States
¶*Department of Chemistry and Biochemistry*
University of California, Santa Barbara, California 93106, United States
§*Department of Chemistry and Biochemistry*
California State University, Fullerton, California 92831, United States
∥*Department of Materials Science and Engineering*
University of California, Los Angeles, California 90095, United States
⊥*Contributed equally to this work*

E-mail: tolbert@chem.ucla.edu; seshadri@mrl.ucsb.edu

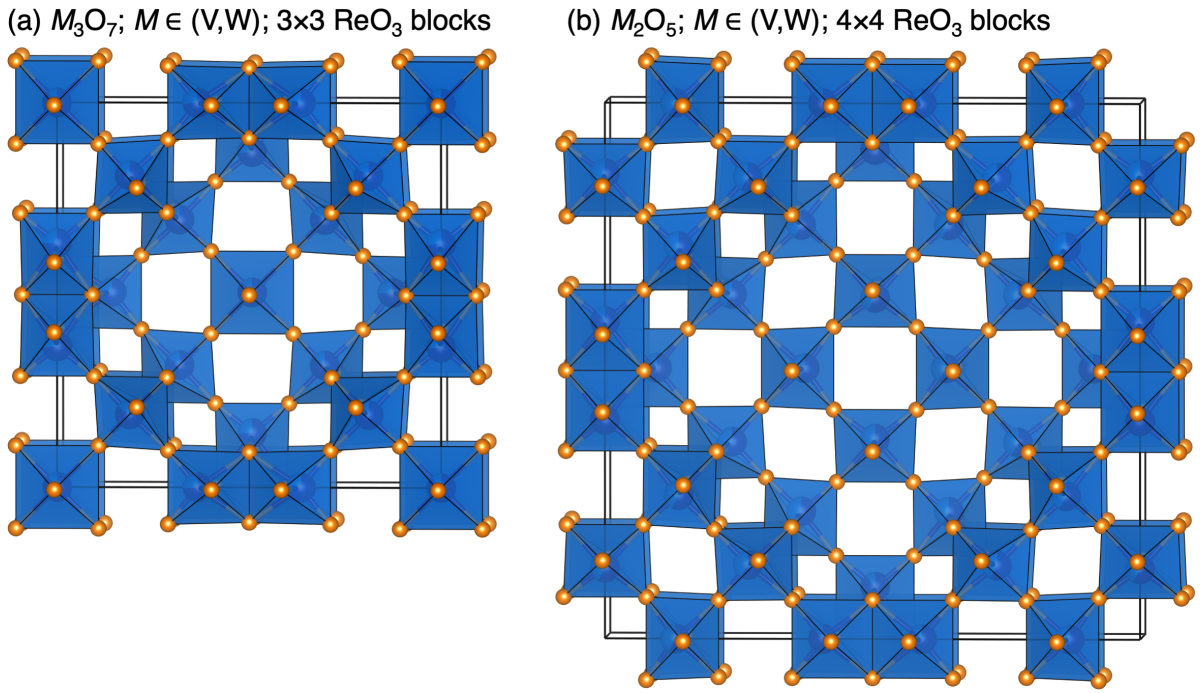

Figure 1: (a) The crystal structure of $(W_{0.2}V_{0.8})_3O_7$ is comprised of 3×3 blocks of octahedra, offset and connected through edge-sharing shear planes. The space group is $I4/mmm$. (b) The crystal structure of $(W_{0.35}V_{0.65})_2O_5$is comprised of 4×4 blocks of octahedra, offset and connected through edge-sharing shear planes. The space group is also $I4/mmm$.

Table 1: Summary of refinement parameters from Figure 2 in the main text for Conv. $(W_{0.2}V_{0.8})_3O_7$.

$(W_{0.2}V_{0.8})_3O_7$		$(W_{0.35}V_{0.65})_2O_5$	
parameter	value	parameter	value
lattice constant	a = 14.00277(3) Å c = 3.71467(2) Å	lattice constant	a = 19.55304(8) Å c = 3.70849(7) Å
space group	I_4/mmm	space group	I_4/mmm
block size	3×3	block size	4×4
percent	91%	percent	9%
R_{wp}	13.91		
R_{exp}	6.21		
GOF = R_{wp}/R_{exp}	2.24		

Table 2: Summary of refinement parameters from Figure 2 in the main text for FD $(W_{0.2}V_{0.8})_3O_7$.

$(W_{0.2}V_{0.8})_3O_7$	
parameter	value
lattice constant	a = 14.01155(5) Å c = 3.71502(9) Å
space group	I_4/mmm
block size	3×3
percent	100%
R_{wp}	12.30
R_{exp}	6.47
GOF = R_{wp}/R_{exp}	1.90

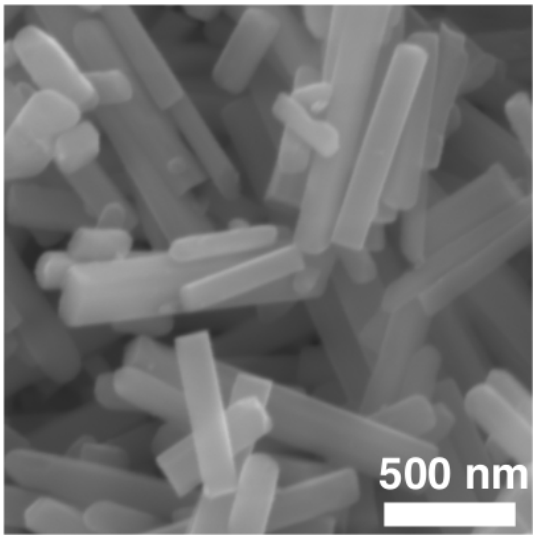

Figure 2: Higher magnification image of pristine FD material.

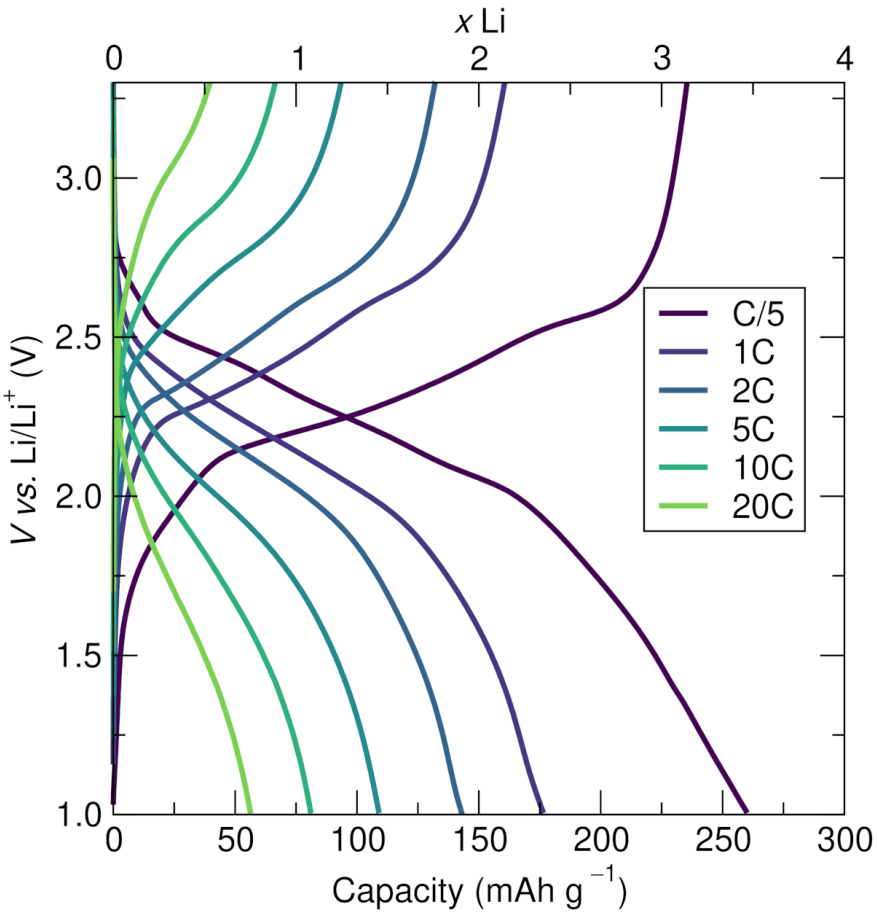

Figure 3: Galvanostatic cycling of Conv. $(W_{0.2}V_{0.8})_3O_7$ at rates from C/5 to 20C.

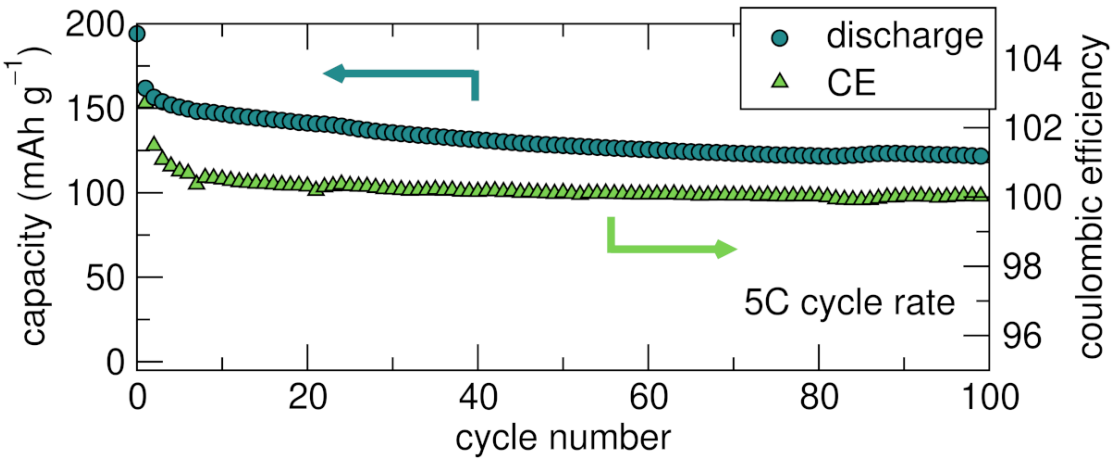

Figure 4: Extended cycling of Conv. $(W_{0.2}V_{0.8})_3O_7$ at a 5C rate.

Table 3: Summary of analysis of the exponent b from Figure 6 that shows the corresponding equations and coefficient of determination that fit the relationship between current and sweep rate for $(W_{0.2}V_{0.8})_3O_7$.

	avg.	b	$\mathbf{R}^2$
red	2.01 V	0.49	0.9975
	2.41 V	0.67	0.9963
ox	2.46 V	0.50	0.9968
	2.69 V	0.61	0.9975

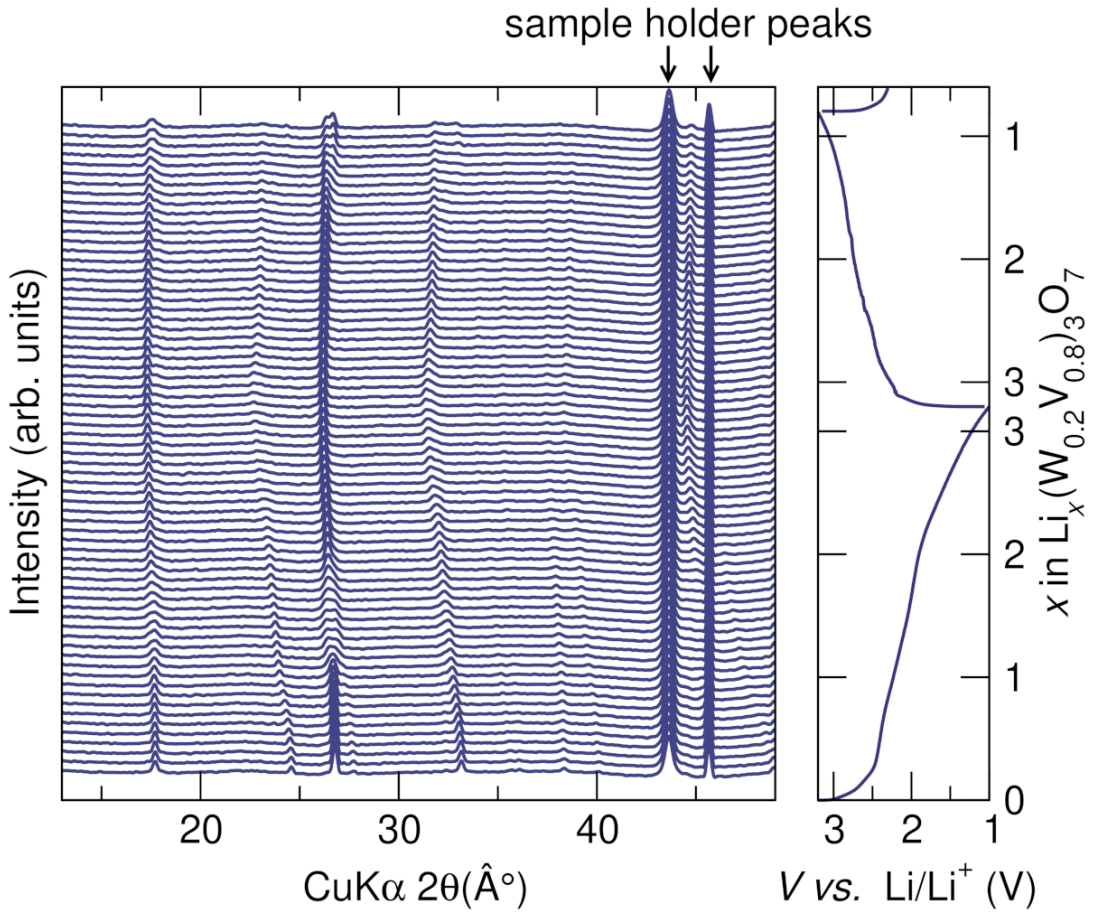

Figure 5: (left) Full *operando* diffraction range of FD $(W_{0.2}V_{0.8})_3O_7$ during the first galvanostatic cycle at a rate of C/10. Electrochemistry is shown on the right panel.

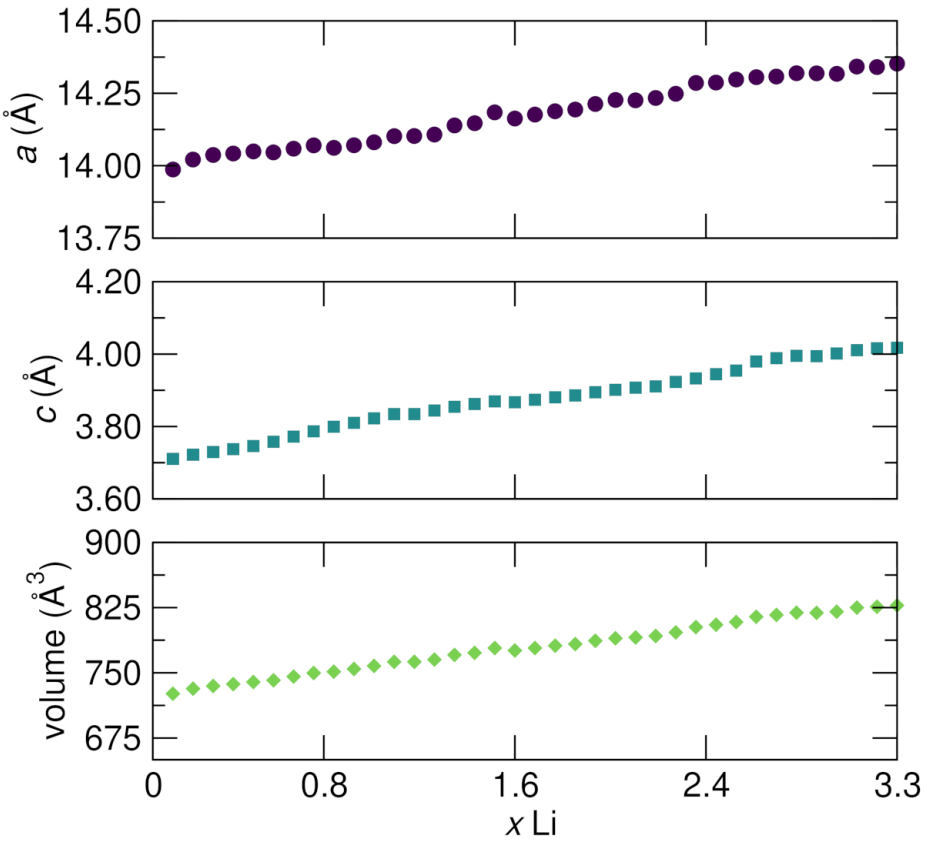

Figure 6: Variation of cell parameters and cell volume with lithiation of the principle 3×3 Wadley-Roth phase of FD $(W_{0.2}V_{0.8})_3O_7$ as a function of lithiation under conditions of *operando* diffraction. A moderate and nearly-linear increase in lattice parameters and cell volume is noted with increasing lithiation.

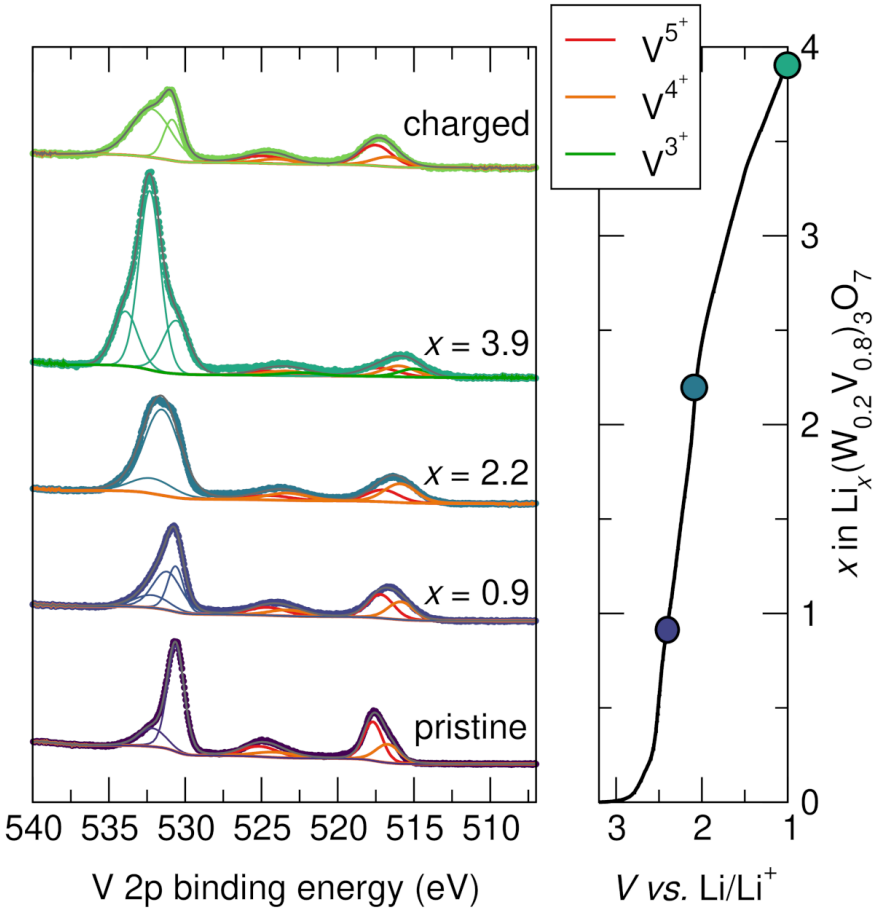

Figure 7: (left) Expanded view showing the full spectral regions for V $2p$ and O $1s$ from XPS. To improve accuracy, all states were fit together. The states of charge are mapped on the electrochemistry shown in the right panel.

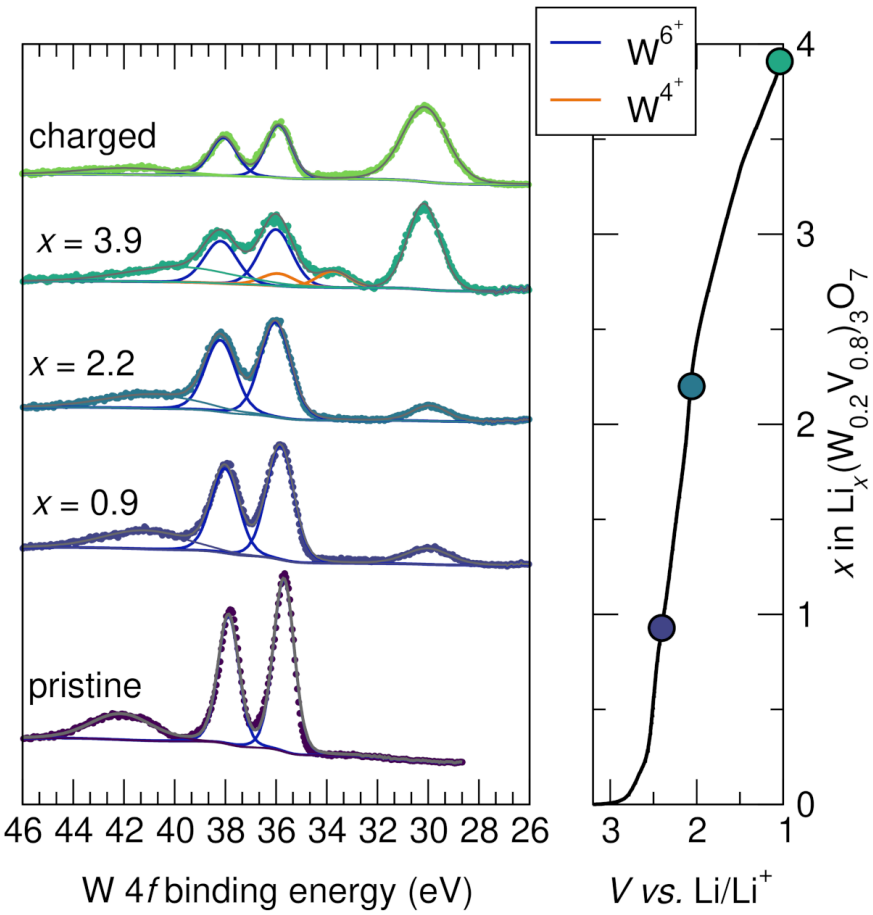

Figure 8: (left) Expanded view showing the full spectral regions for W $4f$ and F $1s$ from XPS. To improve accuracy, all states were fit together. The states of charge are mapped on the electrochemistry shown in the right panel.

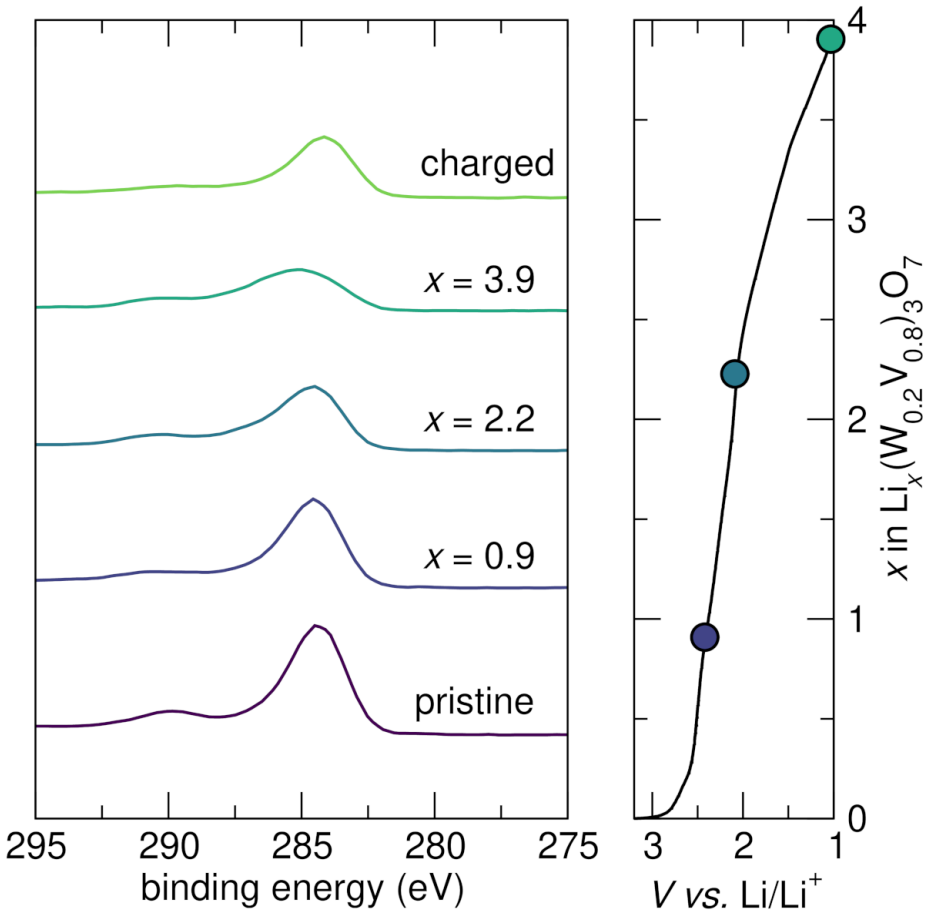

Figure 9: (left) XPS survey scans for each state of charge showing that the C 1s region lines up using the calibration method described in the main text. The states of charge are mapped on the electrochemistry shown in the right panel.

Table 4: Quantitative analysis of the evolution of oxidation states from fitting the high resolution spectra found in Figure 8 and Figure 9.

x in $Li_x(W_{0.2}V_{0.6})_3O_7$	% V^{5+}	% V^{4+}	% V^{3+}	% W^{6+}	% W^{4+}
0	63	37	0	100	0
0.91	57	43	0	100	0
2.15	39	61	0	100	0
3.94	35	38	27	77	23
charged	67	33	0	100	0

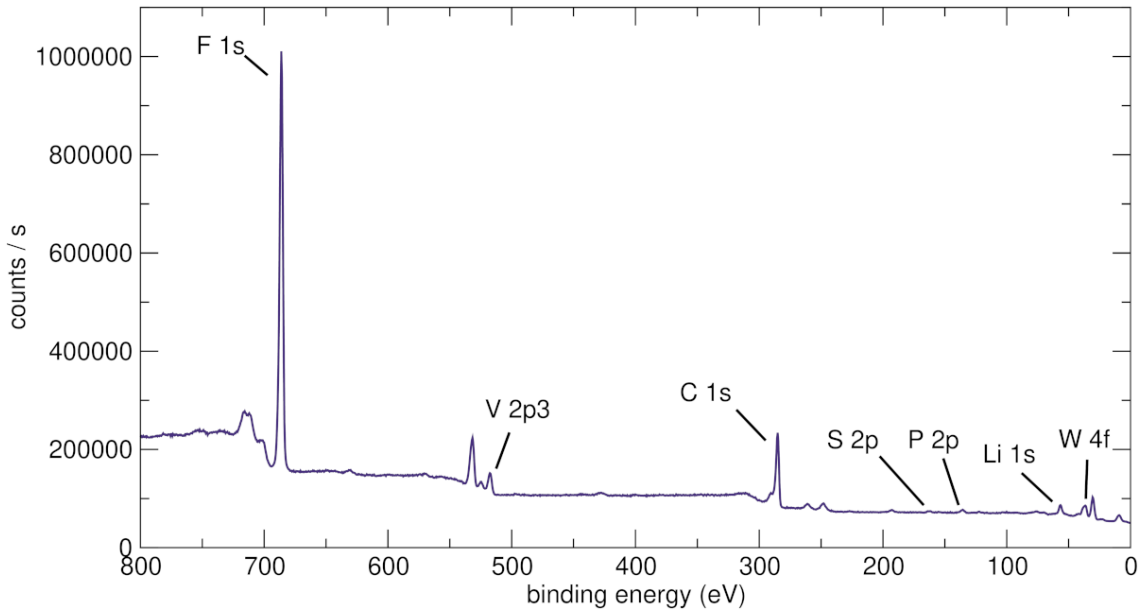

Figure 10: XPS survey scan of a fully discharged electrode shows signals from F $1s$, V $2p3$, C $1s$, S $2p$, P $2p$, Li $1s$, and W $4f$.

Table 5: Quantitative analysis of the elemental composition in an electrode from fitting the survey scan in Figure S10.

Peak	Peak binding energy (eV)	Atomic %
F 1s	685.97	39.64
V 2p3	517.21	1.06
C 1s	285.04	23.33
S 2p	162.00	0.27
P 2P	135.55	0.77
Li 1s	56.51	34.66
W 4f	36.55	0.27

	Expected	Measured
V:W ratio	4.0	3.93

Table 6: Quantitative analysis of the elemental composition from energy-dispersive X-ray spectroscopy in the pristine Conv. material.

Element	Expected atomic fraction	Measured atomic fraction
W	0.20	0.21
V	0.80	0.79